



ELSEVIER

Contents lists available at ScienceDirect

# Medical Image Analysis

journal homepage: [www.elsevier.com/locate/media](http://www.elsevier.com/locate/media)

## Personalized mitral valve closure computation and uncertainty analysis from 3D echocardiography



Sasa Grbic<sup>a,\*</sup>, Thomas F. Easley<sup>b</sup>, Tommaso Mansi<sup>a</sup>, Charles H. Bloodworth<sup>b</sup>, Eric L. Pierce<sup>b</sup>, Ingmar Voigt<sup>a</sup>, Dominik Neumann<sup>a</sup>, Julian Krebs<sup>a</sup>, David D. Yuh<sup>c</sup>, Morten O. Jensen<sup>b</sup>, Dorin Comaniciu<sup>a</sup>, Ajit P. Yoganathan<sup>b</sup>

<sup>a</sup>Medical Imaging Technologies, Siemens Healthcare, Princeton, NJ, United States

<sup>b</sup>The Wallace H. Coulter Department of Biomedical Engineering, Georgia Institute of Technology and Emory University, Atlanta, GA, Georgia

<sup>c</sup>Section of Cardiac Surgery, Department of Surgery, Yale University School of Medicine, New Haven, CT, United States

### ARTICLE INFO

#### Article history:

Received 1 July 2015

Revised 22 March 2016

Accepted 30 March 2016

Available online 17 May 2016

#### Keywords:

Mitral valve modeling

Finite-element biomechanical models

### ABSTRACT

Intervention planning is essential for successful Mitral Valve (MV) repair procedures. Finite-element models (FEM) of the MV could be used to achieve this goal, but the translation to the clinical domain is challenging. Many input parameters for the FEM models, such as tissue properties, are not known. In addition, only simplified MV geometry models can be extracted from non-invasive modalities such as echocardiography imaging, lacking major anatomical details such as the complex chordae topology. A traditional approach for FEM computation is to use a simplified model (also known as parachute model) of the chordae topology, which connects the papillary muscle tips to the free-edges and select basal points. Building on the existing parachute model a new and comprehensive MV model was developed that utilizes a novel chordae representation capable of approximating regional connectivity. In addition, a fully automated personalization approach was developed for the chordae rest length, removing the need for tedious manual parameter selection. Based on the MV model extracted during mid-diastole (open MV) the MV geometric configuration at peak systole (closed MV) was computed according to the FEM model. In this work the focus was placed on validating MV closure computation. The method is evaluated on ten in vitro ovine cases, where in addition to echocardiography imaging, high-resolution  $\mu$ CT imaging is available for accurate validation.

© 2016 Elsevier B.V. All rights reserved.

### 1. Introduction

Valvular heart disease (VHD) is a form of cardiovascular disease affecting 2.5% of the US population (Nkomo et al., 2006), where the function of one or multiple valves is impaired. Mitral valve (MV) disease is one of the most frequent forms of VHD (Jones et al., 2001) and can cause heart failure if left untreated (Roger et al., 2011; Stewart et al., 2003; Braunberger et al., 2001). This is especially present in association with MV regurgitation (MR) with a prevalence of 1.84% in the US (Nkomo et al., 2006), where the MV closure is impaired causing regurgitant back-flow of blood from the left ventricle to the left atrium. Treatment of MR often requires MV replacement or repair surgery to sustain or improve heart function. 8.4% of patients undergoing MV replacement and repair surgery require reoperation (Gammie et al., 2009). In recent years, mitral

valve repair (MVR) procedures, where the valve is surgically altered to restore its proper hemodynamic function, are substituting classical valve replacements (Vassileva et al., 2013; Kilic et al., 2013; Borger et al., 2006), showing improved outcomes, lower operative mortality, improved long-term survival, and improved left ventricular function. As the procedures are technically challenging, they require an experienced surgical team to achieve optimal results (Vassileva et al., 2015; Bolling et al., 2010). In choosing the best procedure for a patient, the surgeon is presented with a flaccid, depressurized heart, and must predict the post-operative implications of the procedure on valve physiology once the heart is contracting. Having a framework to explore different surgical repair strategies for an individual patient and virtually compute their immediate outcomes could reduce the reoperation rate and would be a desired tool in current clinical practice, both in terms of training and planning.

Driven by the widespread prevalence of MV diseases, researchers are developing methods to assess MV anatomy from multiple imaging modalities. Subsequently those methods would

\* Corresponding author.

E-mail address: [sasa.grbic@siemens.com](mailto:sasa.grbic@siemens.com) (S. Grbic).

be used to simulate the MV physiology using biomechanical models (Wang and Sun, 2013; Stevanella et al., 2011; Votta et al., 2013; Grbic et al., 2013). However, the process of retrieving the patient-specific geometric model often requires tedious manual interactions which limit the clinical applicability.

In recent years, methods have been proposed to segment the MV using semi-manual or advanced automated algorithms. Ionasec et al. (2010) proposed to automatically delineate the aortic and mitral valve from dynamic transesophageal echocardiography (TEE) and computed tomography (CT). The computational model was later extended to segment the complete valvular apparatus (Grbic et al., 2012). Schneider et al. (2012) proposed to segment the mitral valve annulus from 3D TEE. However, it is not clear how this method would be extended to cope with diseased anatomies. An example is mitral regurgitation where in addition to the mitral valve annulus the anterior and posterior mitral valve leaflets need to be modeled as well. Pouch et al. (2012) proposed a semi-automated method to extract the MV from echocardiography (Echo); however, it relies on a significant amount of manual interactions in order to retrieve the final MV model. MV model extraction was later automated (Pouch et al., 2014). However, their approach relies on the assumption that all Echo acquisitions are generated with the same field of view. In addition, their method was only evaluated on a small set of clinical data.

The derived geometric models of the valve anatomy can be incorporated into finite-element models (FEM), thus biomechanical computations can be performed based on a personalized patient-specific geometry (Mansi et al., 2012). In Kanik et al. (2014) an automated personalization framework for some of the biomechanical model parameters (stiffness and chordae rest length) was introduced using extended Kalman filters. However, the geometric models used as an input to the biomechanical computation rely on a simplified geometrical representation. Personalized chordae geometry can be extracted from MRI (Stevanella et al., 2011) or CT (Wang and Sun, 2013) however due to limitations of in vivo Echo imaging it is not possible to retrieve a personalized chordae topology from Echo. To apply such computational frameworks (Mansi et al., 2012) in clinical practice, the predictive capabilities and limitations of biomechanical models based on simplified geometric models extracted from Echo must be understood and validated.

In vitro simulators (Siefert et al., 2013; Rabbah et al., 2013) are useful as validation tools for biomechanical models. In addition to acquiring Echo images, similar to clinical Echo data, high-resolution micro-computed tomography data ( $\mu$ CT) can be collected of the same anatomy. Thus, if  $\mu$ CT is assumed to be the ground-truth, it could be used to validate both the accuracy of the geometric model in Echo and the accuracy of the computational model which relies on a simplified geometry. A validation framework for MV computational models was previously proposed (Grbic et al., 2015); however, this framework was applied only on two cases and used a simple chordae representation for the biomechanical model which required tedious manual personalization of chordae rest length parameters.

Here, a novel computational model is proposed and validated which can be constructed from Echo imaging capable of modeling MV closure. An in vitro simulator is used to acquire both Echo and  $\mu$ CT. State-of-the-art geometric modeling techniques are used to segment geometrical models from both modalities. From the Echo geometrical model during diastole a biomechanical model is derived to compute MV closure. The biomechanical model is extended with a new model of chordae topology associated with an automated personalization procedure, estimating chordae specific rest length parameters. The framework is illustrated on ten in vitro data sets.

This study advances prior work on MV FEM (Grbic et al., 2015) as follows:

- A novel and comprehensive MV model using two new chordae tendineae models is presented (a denser pseudo-chordae model and a sparse-dense hybrid model) to improve the approximation of the regional connectivity between leaflets and chordae and thickness compared to the sparse model presented in Mansi et al. (2012). The model is applied to both marginal and basal chordae.
- An automated personalization framework is developed based on trust region optimization, eliminating the need for tedious manual personalization of chordae rest length.
- An inter-rater variability study is performed to quantify the geometric uncertainty in the MV geometry from the Echo images and its impact on the simulation result by uncertainty propagation. Results from this experiment can be used to gauge the meaningful range of accuracy for the computational model.
- A sensitivity analysis is performed to identify the most significant parameters of our biomechanical MV FEM for closure computation.
- The validation set is increased to 10 ovine cases (compared to 2 cases in Grbic et al. (2015)).

## 2. Methods

In this section the geometric model parameterization of the computational MV model was introduced, then the biomechanical model was presented including the novel chordae representation and automatic personalization framework. Finally, the in vitro simulator was presented, used for model validation.

### 2.1. Geometric modeling of the mitral valve

An anatomical point distribution model, similar as in (Ionasec et al., 2010; Grbic et al., 2012) was used to represent the MV geometry and its subvalvular apparatus, segmented from 3D Echo. The model was hierarchically parameterized with three layers. On the coarsest layer the global location of the MV was represented as a bounding box. The second layer models the anatomy of the MV with anatomical landmarks. The nine landmarks (two trigones, two commissures, one posterior annulus mid-point, two leaflet tips, and two papillary tips) are representing key anatomical locations and are capable of capturing a broad spectrum of morphological and physiological variations of the MV physiology (Ho, 2002). On the finest layer, the model was comprised of the MV annulus, the anterior and posterior leaflets represented as surface models.

As not enough ovine data sets were available to train a learning based segmentation system, the method in (Grbic et al., 2012) was adapted to manually initialize the MV geometric model in the in vitro Echo images. The user first manually initializes the bounding box of the MV. Then, the user manually positions the MV landmarks (trigones, papillary muscle tips, posterior annulus midpoint, commissures, and leaflet tips). Based on the landmarks a surface model was automatically initialized. Finally, the user manually adjusts the full surface model to the MV structure. A custom Siemens Valve Modeling prototype was used for MV geometry modeling. Fig. 1 depicts the MV model annotation workflow from the Echo images.

### 2.2. Biomechanical model of the mitral valve

An extension of the model proposed in (Mansi et al., 2012) was used to compute the MV closure based on the Echo anatomy. The dynamics system

$$M\ddot{\mathbf{u}} + C\dot{\mathbf{u}} + K\mathbf{u} = \vec{f}_t + \vec{f}_p + \vec{f}_c \quad (1)$$

is solved, where  $M$  was the diagonal mass matrix calculated from the mass density,  $\rho = 1040 \text{ g/L}$ ,  $C$  was the Rayleigh damping matrix with coefficients  $1e4 \text{ s}^{-1}$  and  $0.1 \text{ s}$  for the mass and stiffness

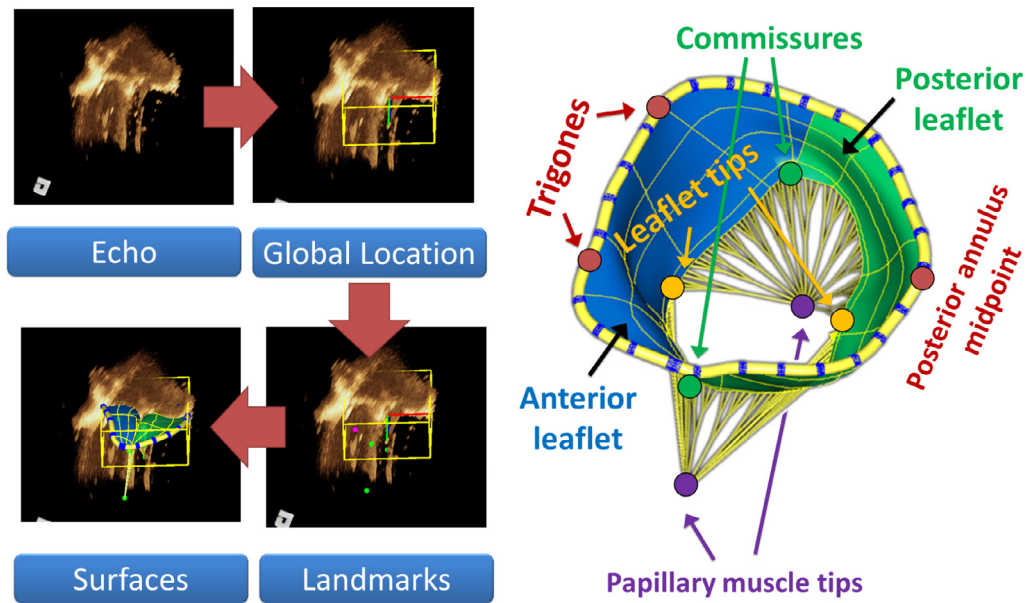


**Fig. 1.** Left) Hierarchical mitral valve modeling approach from an in vitro Echo scan. First, the global position of the mitral valve was manually defined. Anatomical landmarks are then selected. Finally, the anterior and posterior surface models are segmented. Right) Atrial view of the final mitral valve model consisting of the anterior and posterior leaflets and nine landmarks. A parachute model of the marginal chordae tendineae are shown in yellow. (For interpretation of the references to color in this figure legend, the reader is referred to the web version of this article).

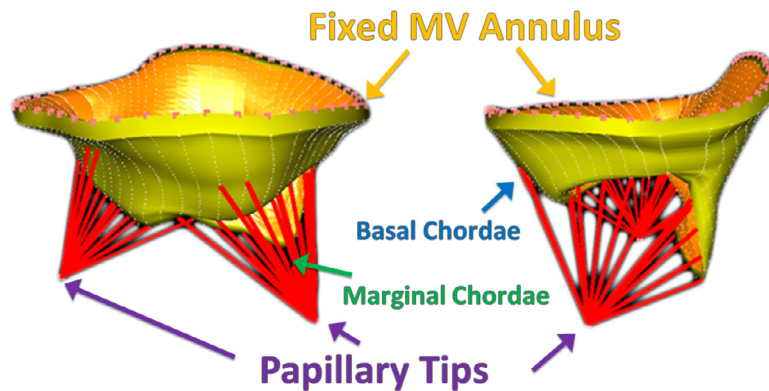


**Fig. 2.** Visualization of the computational FEM of the MV as presented in (Mansi et al., 2012) with the sparse chordae representation.

matrix respectively,  $K$  was the stiffness matrix,  $\vec{f}_t$  was the force created by the chords on the leaflets,  $\vec{f}_p$  the left ventricular pressure force,  $\vec{f}_c$  the contact forces and  $\vec{u}$  the displacement. Transverse isotropic linear tissue elasticity was used within the FEM model, motivated by findings in Kunzelman et al. (1993), implemented using a co-rotational FEM to cope with large deformations (Comas et al., 2008). Poisson ratio was set as  $\nu = 0.488$  for both leaflets, fiber Young's modulus was  $E_{AL} = 6.23$  MPa and  $E_{PL} = 2.09$  MPa for the anterior and posterior leaflets, cross-fiber Young's modulus was  $E_{AL} = 2.35$  MPa and  $E_{PL} = 1.88$  MPa, and shear modulus was 1.37 MPa (Mansi et al., 2012).

An improved chordae representation was proposed for the computational model. The previous approach (Mansi et al., 2012) used the traditional chordae representation where the chordae topology was modeled as 28 marginal chordae evenly spaced along the free-edges of the leaflets and 4 basal chordae, tethered at the base of the leaflets on the ventricular side (Fig. 2). The number of pseudo-chordae was defined by the MV mesh resolution. As each chordae was attached to only one vertex, the load distribution on the leaflet was not modeled properly due to the lack of thickness and secondary chordae representation. Two novel representations of chordae topology were proposed: 1) a dense pseudo-

chordae representation and 2) hybrid sparse-dense pseudo-chordae representation.

**Dense pseudo-chordae model:** The sparse chordae representation was disentangled in (Mansi et al., 2012) for computational purposes into smaller elements by adding pseudo-chordae to each vertex on the ventricular side of the MV leaflet mesh to the related papillary tip (Fig. 3). 87 marginal pseudo-chordae were used instead of the 28 used in Mansi et al. (2012) and 1500 basal pseudo-chordae instead of 4. The number of pseudo-chordae was defined by the MV mesh resolution. Thus a group of pseudo-chordae, representing tensile spring elements, was approximating chordae with a larger thickness. The pseudo-chordae were only active if their length was above the rest length. MV annulus and papillary muscle points were fixed during the computation for both chordae models.

**Hybrid sparse-dense pseudo-chordae model:** Instead of connecting a chordae only to one vertex on the leaflet, as done with the sparse representation (Mansi et al., 2012), each chordae was connected to a small patch (see Fig. 4). In the new model, each leaflet contained two basal patches with each having 18 pseudo-chordae connecting to one papillary muscle tip. In total there were 72 basal pseudo-chordae. The number of marginal pseudo-chordae was 87, same as for the dense model. A group of tensile spring

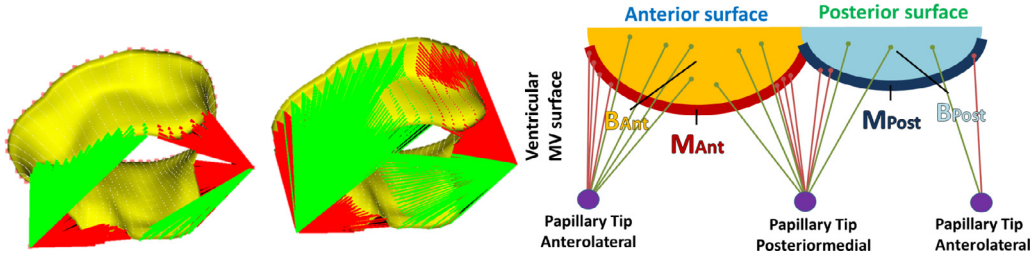


**Fig. 3.** (Left, middle) Computational model with dense pseudo-chordae representation modeled as tensile springs; (right) image is showing the subdivision of the four regions among the anterior and posterior leaflet ( $B_{Ant}$ ,  $M_{Ant}$ ,  $B_{Post}$ ,  $M_{Post}$ ).

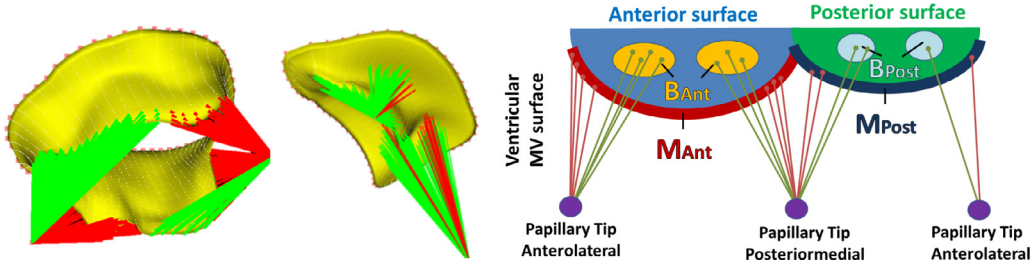


**Fig. 4.** (Left, middle) Computational model with hybrid sparse-dense regional pseudo-chordae representation modeled as tensile springs; (right) image was showing the subdivision of the four regions among the anterior and posterior leaflet ( $B_{Ant}$ ,  $M_{Ant}$ ,  $B_{Post}$ ,  $M_{Post}$ ).

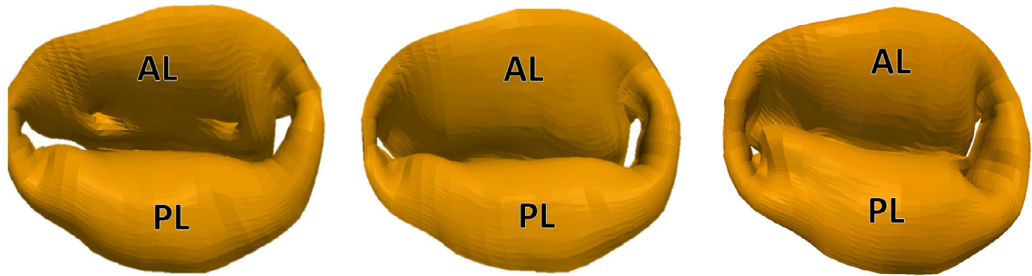


**Fig. 5.** Comparison of computed closure geometry based on the old sparse chordae model (Mansi et al., 2012) (left) and the two improved dense chordae representations: (middle) dense pseudo-chordae model; (right) hybrid sparse-dense pseudo-chordae model Atrial View. AL: anterior MV leaflet and PL: posterior MV leaflet. All MV model configurations were obtained after chordae rest length personalization. The tethering of chordae and discrete leaflet vertices is clearly visible in the sparse model.

elements was used to approximate chordae thickness and secondary chordae attachments. As seen later in Fig. 5 the bulging of the anterior and posterior leaflet does not show tethering artifacts for the improved models compared to the previous approach.

For all chordae representations an inverse modeling framework was developed based on trust region optimization (Powell, 2009) to estimate the chordae rest length. Hereby, the chordae representation was divided into four regions according to their attachment on the anterior and posterior leaflet ( $B_{Ant}$  - anterior leaflet basal chordae,  $M_{Ant}$  - anterior leaflet marginal chordae,  $B_{Post}$  - posterior leaflet basal chordae,  $M_{Post}$  posterior leaflet marginal chordae), as shown in Figs. 3 and 4. To avoid having the same rest length for all tensile springs within one region their specific rest length was adjusted based on the following formula

$$rl_x = \left(1 + \frac{x-s}{l-s}\right) rl_{optimized} \quad (2)$$

where  $rl_x$  was the rest length of an individual tensile spring,  $x$  was representing the distance between the papillary tip to vertex distance,  $s$  the shortest distance between the papillary tip and any vertex in the leaflet region,  $l$  the longest distance between the papillary tip and any vertex in the leaflet region, the rest length multiplier for each of the four leaflet regions. All measurements were computed from the MV model during mid-diastole (MV open). Hereby the BOBYQA (Bound Optimization by Quadratic Approximation) algorithm (Powell, 2009) is utilized, a gradient-free opti-

mization framework to optimize the chordae rest length for each of the four regions  $rl_{optimized}$ . The following cost function was used to determine parameter updates for the next iteration:

$$CF = d_{ptm} \quad (3)$$

The point-to-mesh geometric difference  $d_{ptm}$  was used to quantify the goodness of fit of the computed closure model  $S'$  with respect to the observed peak systolic MV model from Echo S. The symmetric point-to-mesh error between the surfaces  $S$  and  $S'$  was defined as follows:

$$d_{ptm}(S, S') = \frac{d(S, S') + d(S', S)}{2} \quad (4)$$

with

$$d(S, S') = \frac{1}{|S|} \int_{p \in S} d(p, S') dS \quad (5)$$

where  $d(p, S')$  denotes the shortest distance of point  $p$  belonging to surface  $S$  to the surface  $S'$  (Aspert et al., 2002).

The cost function was determined by the difference between the MV model at peak systole  $S$  and the simulated MV closure model  $S'$  based on the biomechanical model, once the equilibrium position was reached. It is important to note that the parameters were optimized with respect to the MV model at peak systole, thus, if incongruent closure was observed at peak systole, the model would adjust the internal parameter of the computational

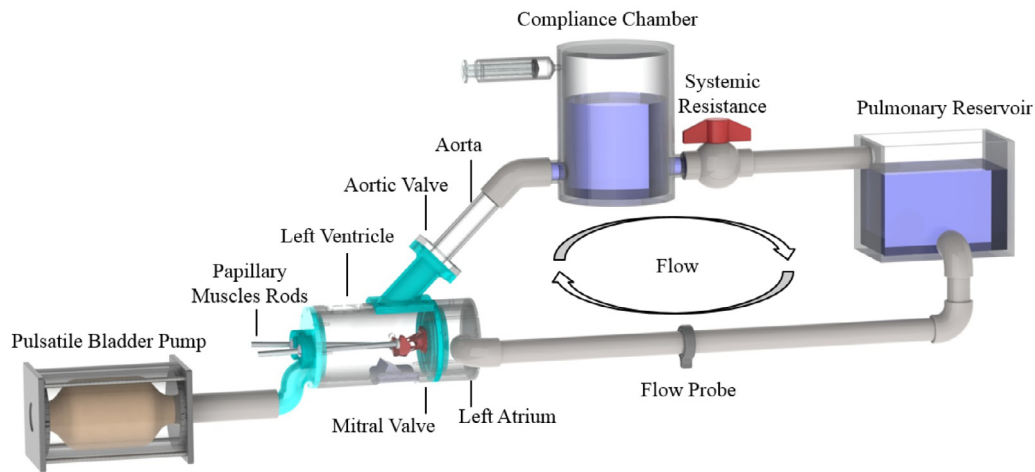


Fig. 6. Schematic of the Georgia Tech Left Heart Simulator (GTLHS) with components identified.

model to match the MV geometry. During the iterative optimization (BOBYQA), the optimal values (chordae rest lengths for each region) of the biomechanical model were determined iteratively. Self-collisions were modeled with collision stiffness of 100 kPa and friction coefficient of 0.1 (Mansi et al., 2012). The SOFA (Simulation Open Framework Architecture) framework (Allard et al., 2007) was used to implement the MV biomechanical model. A closure computation takes approximately 30 s.

The same manual hierarchical modeling approach was utilized to model the MV geometry for the  $\mu$ CT images.

### 2.3. In vitro validation setup

In order to validate the framework the Georgia Tech Left Heart Simulator (GTLHS) (Siefert et al., 2013; Rabbah et al., 2013; Jimenez et al., 2005) was utilized (Fig. 6). A program written in LabVIEW (National Instruments; Austin, TX) was used to control the pulsatile bladder pump and to measure left ventricle and left atrial pressures and MV flow. The pump was used to create systolic and diastolic, pressure and flow. The flow was measured using an electromagnetic flow probe, and pressures were measured using wall-tapped pressure transducers. In addition, a bi-leaflet mechanical heart valve was used in place of the aortic valve. This in vitro model was idealized in that it was rigid-walled and has a static MV annulus. Overall, the GTLHS consists of a controlled in vitro environment where MV structure and function could be studied through multiple imaging modalities. In addition to Echo, a high resolution  $\mu$ CT image could be acquired, allowing for high structure detail of the MV anatomy that was not achievable with clinical imaging techniques. The pressurized  $\mu$ CT was used to extract ground truth geometry of the closed MV.

**Preparation:** Healthy ovine hearts were obtained through a local supplier, and the MV was excised, preserving its annular and subvalvular anatomy. The valves were then mounted to the annulus holder and the mechanical papillary muscle (PM) positioning system (rods) of the GTLHS.

**Echo imaging:** 3D+t Echo imaging of the MV mounted within the LHS was performed using an ie33 xMatrix ultrasound system and x7-2 probe (Philips Healthcare; Andover, MA). 3D images of the entire mitral complex, including annulus, leaflets, chordae, and PM were acquired. The region of interest was adjusted to the smallest pyramid volume that encompassed the entire mitral complex to maximize frame rate. For processing the acoustic 3D image from the x7 probe was converted to an isotropic volume in Cartesian coordinates with 0.5 mm isotropic resolution.

**$\mu$ CT imaging:** Following in vitro Echo, the GTLHS was drained of saline and mounted into the Inveon  $\mu$ CT System for  $\mu$ CT imaging (Siemens Medical Solutions USA, Inc.; Malvern, PA). The dataset had a spatial resolution of 43.29  $\mu$ m voxel size, and captured the entire MV in its field of view. The scan was conducted in air with parameters optimized for soft tissue. In order to hold the MV closed and static, steady air pressure was delivered to the left heart chamber via air lines from an external air compressor.

## 3. Experimental results

The framework was evaluated on ten ovine valves. In Section 3.2 a geometric comparison was performed between the MV models from Echo and  $\mu$ CT (considered ground truth) during peak systole (closed MV). To quantify the ambiguity of the manually segmented geometric MV models in the Echo images an inter-rater variability analysis was performed in Section 3.3. In Section 3.4 a sensitivity analysis was done on the biomechanical FEM MV model to determine the most important parameters for personalization. Finally, in Section 3.5 the MV closure computation was validated. From an in vitro mid-diastolic Echo image (MV open) the MV geometry was manually segmented. The MV FEM was used to compute the MV geometry configuration during peak systole (MV closed). The computed MV geometry configuration was then compared to the ground truth geometrical configuration obtained from the  $\mu$ CT image (see Fig. 7). Within the validation workflow the three MV FEM models (MV FEM models with 1) sparse, 2) dense and 3) hybrid sparse-dense pseudo-chordae representation) could be interchanged.

### 3.1. Mitral valve dimension

The dimensions of the ten in-vitro mitral valves was quantified with two measurements: 1) inter-commissure distance and 2) antero-posterior diameter. For the inter-commissure the mean distance was 27.55 mm ( $\pm$  2.53 mm) and 21.76 mm ( $\pm$  2.52 mm) for the antero-posterior diameter. More details are provided in Fig. 8.

### 3.2. Geometric comparison

Prior work only used one modality, 3D TEE, (Mansi et al., 2012) for both constructing biomechanical MV models and validating them. As a multi-modal approach was used where the Echo images were used for modeling and  $\mu$ CT for validation, it was important to understand what the intrinsic geometric difference was

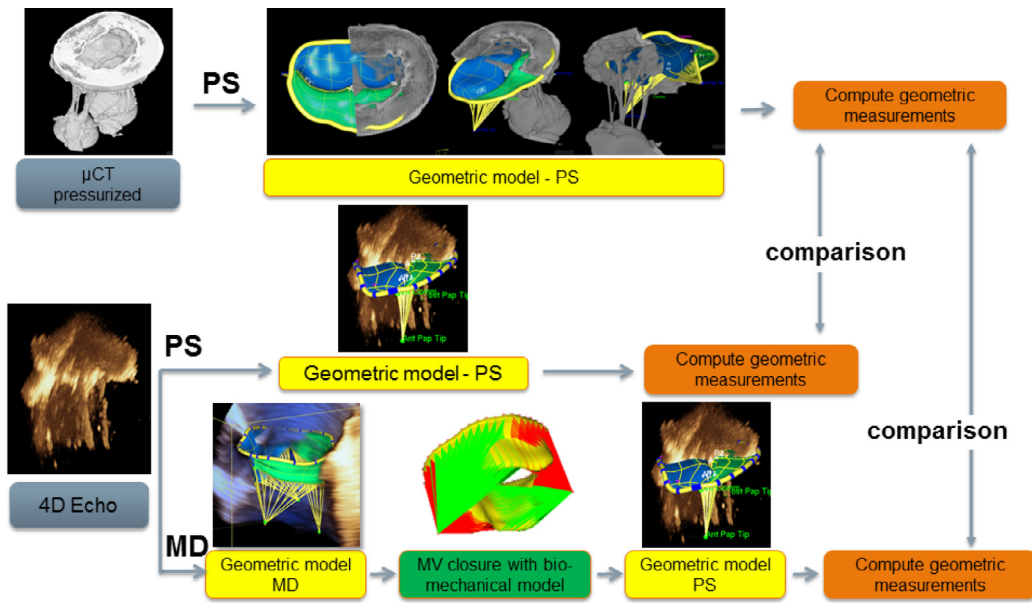
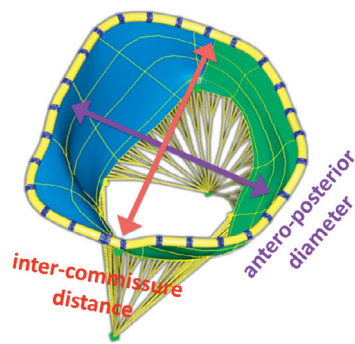


**Fig. 7.** The proposed workflow for MV closure computation validation. Starting from an in vitro Echo image at mid-diastole the geometric model of the MV apparatus was manually segmented. The open MV model was closed according to the biomechanical model and the result validated against the ground-truth MV model extracted from a pressurized  $\mu$ CT scan. PS - peak systole, MD - mid diastole.



Data Set	Inter-Commissure Distance (mm)	Antero-Posterior Diameter (mm)
1	29.32	22.00
2	28.25	20.78
3	25.53	19.81
4	29.32	19.64
5	30.21	18.57
6	31.16	21.81
7	27.03	24.68
8	26.37	23.01
9	25.31	20.44
10	23.07	26.85
Average	$27.55 \pm 2.53$	$21.76 \pm 2.52$

**Fig. 8.** Quantification of ten mitral valve models by calculating the inter-commissure distance and the antero-posterior diameter. The measurements are calculated from the  $\mu$ CT model.

between the MV models extracted from each modality. Those differences were mostly due to the ambiguity in the Echo annotation, but as the computational model will be personalized only using Echo it was important to understand what would be the minimal achievable error. Thus the difference between the MV model extracted from Echo and  $\mu$ CT was quantified. The average point-to-mesh distance between the peak systolic Echo MV model (Echo) and  $\mu$ CT model were shown in Table 1. Detailed point-to-mesh errors across the complete MV surface for the complete data set can be seen in Fig. 9.

**Table 1**

Mean point-to-mesh distance and standard deviation between the peak systolic Echo MV model (Echo) and  $\mu$ CT model. The average error is  $0.97 \pm 0.15$  mm.

Data Set	Point-to-Mesh Error (mm)	Data Set	Point-to-Mesh Error (mm)
01	$1.18 \pm 0.77$	06	$0.89 \pm 0.60$
02	$1.17 \pm 0.78$	07	$0.93 \pm 0.69$
03	$0.84 \pm 0.59$	08	$1.12 \pm 0.78$
04	$0.92 \pm 0.73$	09	$1.01 \pm 0.81$
05	$0.69 \pm 0.58$	10	$1.03 \pm 0.70$

### 3.3. Inter-rater variability

To quantify the geometric uncertainty in the MV geometry from the Echo images an inter-rater variability study was performed with four raters with 10 data sets. Manual annotations of the MV model were performed in the Echo images in both mid-diastole and peak systole. The model from rater 1 was obtained using the manual process described in Section 2. For raters 2–4 a random perturbation of the MV model from rater 1 was

generated. The resulting initial models had a variability of more than 4.5 mm point-to-mesh error when compared to the ground-truth model from  $\mu$ CT. The raters 2–4 manually changed this perturbed model using the Siemens Valve Modeling Prototype to align it to the Echo images. The raters could change both the surfaces and landmarks. The raters were expert users with more than two years of experience working with cardiac ultrasound.

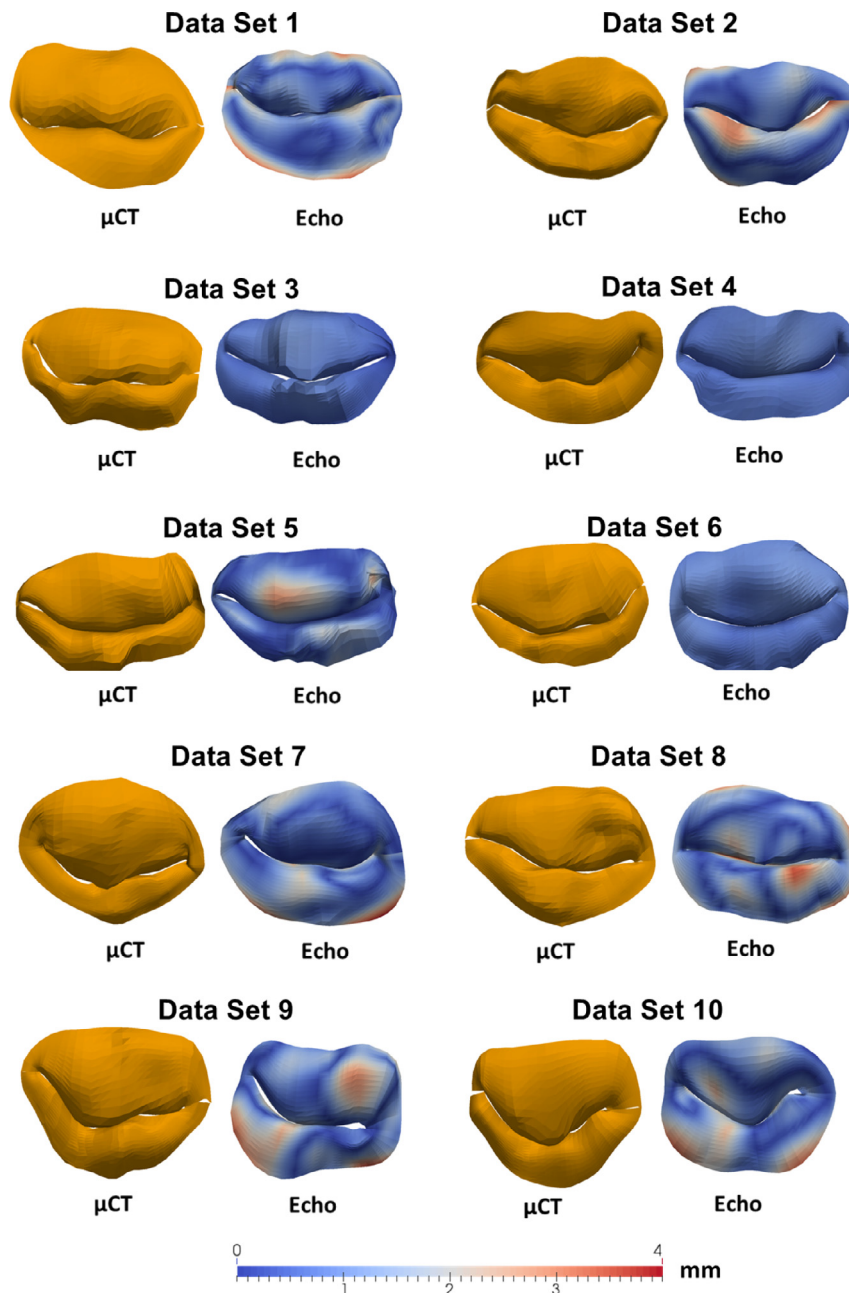


Fig. 9. Qualitative comparison of MV geometry from ventricular Echo (Echo) compared to the ground-truth CT model. Point-to-mesh distance was color-coded on the Echo model.

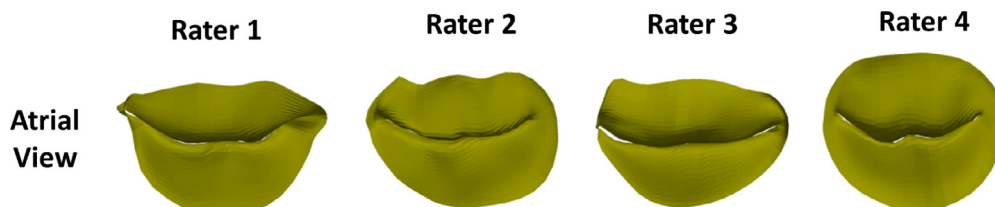


Fig. 10. Qualitative comparison of mitral valve model annotations of four raters from peak systolic Echo images for one data set (atrial view).

Examples of the MV model from the four raters are shown in Fig. 10.

First, the ground truth model was assumed to be the mean model of all raters. As all MV annotations preserve point-correspondences this step consisted of averaging each vertex over all users. Then the geometric differences between each

user and the mean model were calculated. Average point-to-mesh error between the mean model and the user annotations for all 10 data sets was  $1.38 \pm 0.47$  mm. The 95% error was 2.30 mm. In the second experiment, the ground truth model was assumed to be the MV model from  $\mu$ CT and for each data set the average distance was computed between the four rater MV models and

the registered  $\mu$ CT model. Average point-to-mesh error was  $1.66 \pm 0.47$  mm. The 95% error was 2.58 mm.

### 3.4. Sensitivity analysis

A sensitivity analysis of the main biomechanical parameters was carried out to identify the most important parameters when calibrating the MV FEM. The effects of parameter selection was evaluated with respect to the computed MV closure by successively varying one parameter and fixing the remaining parameters to standard values (as described in the methods section). To quantify the sensitivity of the closure model during the computation, the leaflet tip-annulus distance was selected for both the anterior and posterior MV leaflets. The following MV FEM parameters were varied: pressure, MV geometry, and Young's Modulus. For the ventricular pressure  $f_p$ , a generic pressure profile was defined with a maximum value of  $f_{pmax} = 120$  mmHg. This pressure profile was then scaled where the maximum value  $f_{pmax}$  was varied from  $-50\%$  to  $+50\%$  of the standard value of 120 mmHg. Fig. 11a and b shows the impact of different pressure profiles on the MV closure model. We used the geometric model from rater one for the experiment. To assess the impact of MV geometry variability with respect to the closure computation, the MV geometry from the four raters from the inter-rater variability experiment was used from Data Set 1. The chordae rest length parameters of the biomechanical model were personalized for each model individually. The impacts on the MV closure configuration was shown in Fig. 11c and d. For the Young's Moduli the standard values ( $E_{AL} = 6.23$  MPa,  $E_{PL} = 2.09$  MPa) were varied from  $-50\%$  to  $+50\%$  simultaneously. The cross-fiber Young's modulus ( $G_{AL}$ ,  $G_{PL}$ ) and shear modulus were varied at the same time by keeping a fixed ratio:  $G_{AL} = 0.21 * E_{AL}MPa$ ,  $G_{PL} = 0.33 * E_{PL}MPa$ . The parameter ratios were derived from the default values proposed in (Schievano et al., 2009). The results were shown in Fig. 11e for the anterior leaflet and 11 f for the posterior leaflet.

The experiments with chordae rest length personalization were omitted as the study in (Mansi et al., 2012) had already shown that chordae rest length had a significant impact on MV closure (Mansi et al., 2012). Thus the chordae rest length parameters were personalized per region ( $B_{Ant}$ ,  $M_{Ant}$ ,  $B_{Post}$ ,  $M_{Post}$ ) in all of the experiments using inverse modeling techniques. As both the dense pseudo-chordae model and the hybrid sparse-dense pseudo-chordae model showed similar behavior in the sensitivity analysis after chordae rest length personalization, only experimental results with the hybrid sparse-dense pseudo-chordae model were shown.

### 3.5. MV closure computation

MV closure was computed using the biomechanical model starting from the mid-diastolic Echo MV model (open MV). The chordae rest lengths per region ( $B_{Ant}$ ,  $M_{Ant}$ ,  $B_{Post}$ ,  $M_{Post}$ ) were automatically personalized in a coarse-to-fine approach using the BOBYQA algorithm. Finally, to capture the fast dynamics and correctly account for collisions and inertia, pressure increase duration was scaled to last 10 s and 1000 iterations were calculated. Fig. 12 illustrates the geometric distance between the simulated Echo closure (Sim Echo) model compared to the ground-truth  $\mu$ CT model. The average point-to-mesh error was shown in Table 2 and Fig. 12. Using a two-tailed, paired sample t-test, it was found that the dense chordae model ( $p < 0.005$ ) and hybrid chordae model ( $p < 0.005$ ) were significantly different from the sparse chordae model.

**Table 2**

Mean point-to-mesh distance  $\pm$  standard deviation (95th percentile error comparison) between the ground-truth  $\mu$ CT mitral valve (MV) model at peak systole and simulated closure model computed using the MV biomechanical model with sparse, dense and hybrid sparse-dense pseudo-chordae representation. The dense and hybrid chordae model results differed significantly from the sparse model ( $p < 0.005$ ).

Data Set	Sparse Chordae Model Point-to-Mesh Error (mm)	Dense Chordae Model Point-to-Mesh Error (mm)	Hybrid Chordae Model Point-to-Mesh Error (mm)
01	$3.22 \pm 1.61$ (6.75)	$2.48 \pm 1.44$ (5.36)	$2.37 \pm 1.31$ (4.98)
02	$3.92 \pm 1.95$ (7.92)	$3.11 \pm 1.63$ (6.25)	$3.05 \pm 1.64$ (6.17)
03	$2.73 \pm 1.98$ (7.05)	$2.94 \pm 2.11$ (7.07)	$2.95 \pm 2.12$ (7.10)
04	$2.57 \pm 1.85$ (6.63)	$1.56 \pm 1.02$ (3.58)	$1.54 \pm 1.17$ (3.79)
05	$2.11 \pm 1.61$ (5.24)	$1.63 \pm 1.01$ (3.72)	$1.57 \pm 1.06$ (3.66)
06	$2.73 \pm 1.61$ (5.94)	$2.06 \pm 1.22$ (4.71)	$2.03 \pm 1.32$ (4.65)
07	$2.38 \pm 1.29$ (5.03)	$1.89 \pm 1.12$ (4.05)	$1.85 \pm 1.10$ (4.01)
08	$2.28 \pm 1.55$ (5.59)	$2.08 \pm 1.34$ (4.65)	$2.02 \pm 1.31$ (4.54)
09	$2.64 \pm 1.73$ (5.93)	$2.53 \pm 1.56$ (5.65)	$2.52 \pm 1.53$ (5.61)
10	$2.58 \pm 1.49$ (5.71)	$2.21 \pm 1.35$ (4.87)	$2.23 \pm 1.32$ (4.84)
Average	$2.71 \pm 0.51$	$2.24 \pm 0.52$	$2.21 \pm 0.51$

### 3.6. Personalization

In this section we determined the importance of chordae rest length personalization for MV closure computation. The geometric difference of the computed closure model with personalized rest length parameters ( $B_{Ant}$ ,  $M_{Ant}$ ,  $B_{Post}$ ,  $M_{Post}$ ) was compared to a model with generic values. The generic chordae rest length was selected to be the mean chordae rest length of all personalized models for all four chordae regions,  $B_{Ant} = M_{Ant} = B_{Post} = M_{Post} = 11.06$  mm. The hybrid sparse-dense pseudo-chordae representation was used in the experiments as they produce the most accurate closure configurations while being physiologically meaningful. Mean point-to-mesh distance comparing the results to the ground truth  $\mu$ CT model are shown in Fig. 13.

During the trust region optimization, the cost function was reduced to achieve optimal closure results. Fig. 14 shows the cost function over several iterations for four data sets.

## 4. Discussion

A validated MV surgery planning framework could open new avenues in the technical and clinical space of MV surgery planning. In this work, an integrated approach was proposed consisting of state-of-the-art geometric modelling techniques and a novel biomechanical model capable of computing MV closure accurately. As only simplified MV geometric models could be extracted from Echo, in vivo biomechanical models based on the simplified geometry (Mansi et al., 2012) cannot be applied in clinical practice without comprehensive validation. The GTLHS was utilized which could acquire high resolution  $\mu$ CT imaging in addition to Echo. Thus accurate geometric models could be extracted for validation. In addition, multiple parameters, such as pressures, could be measured in the setup and were used within the computational model. As the chordae rest lengths have a significant effect on MV closure (Mansi et al., 2012), an automated approach was proposed to optimize the rest length parameters of the biomechanical model, eliminating the need for tedious manual personalization of chordae rest length.

As the thickness of primary and secondary chordae is not explicitly represented, the dense pseudo-chordae and hybrid sparse-dense pseudo-chordae model could be seen as a compromise of modeling the thickness of both the primary and secondary chordae as tensile springs. As the full chordae topology is not observable in Echo, this representation is a simple and viable alternative. In comparison to the previous chordae model (Mansi et al., 2012), the bulging of the leaflets appears more natural by utilizing the

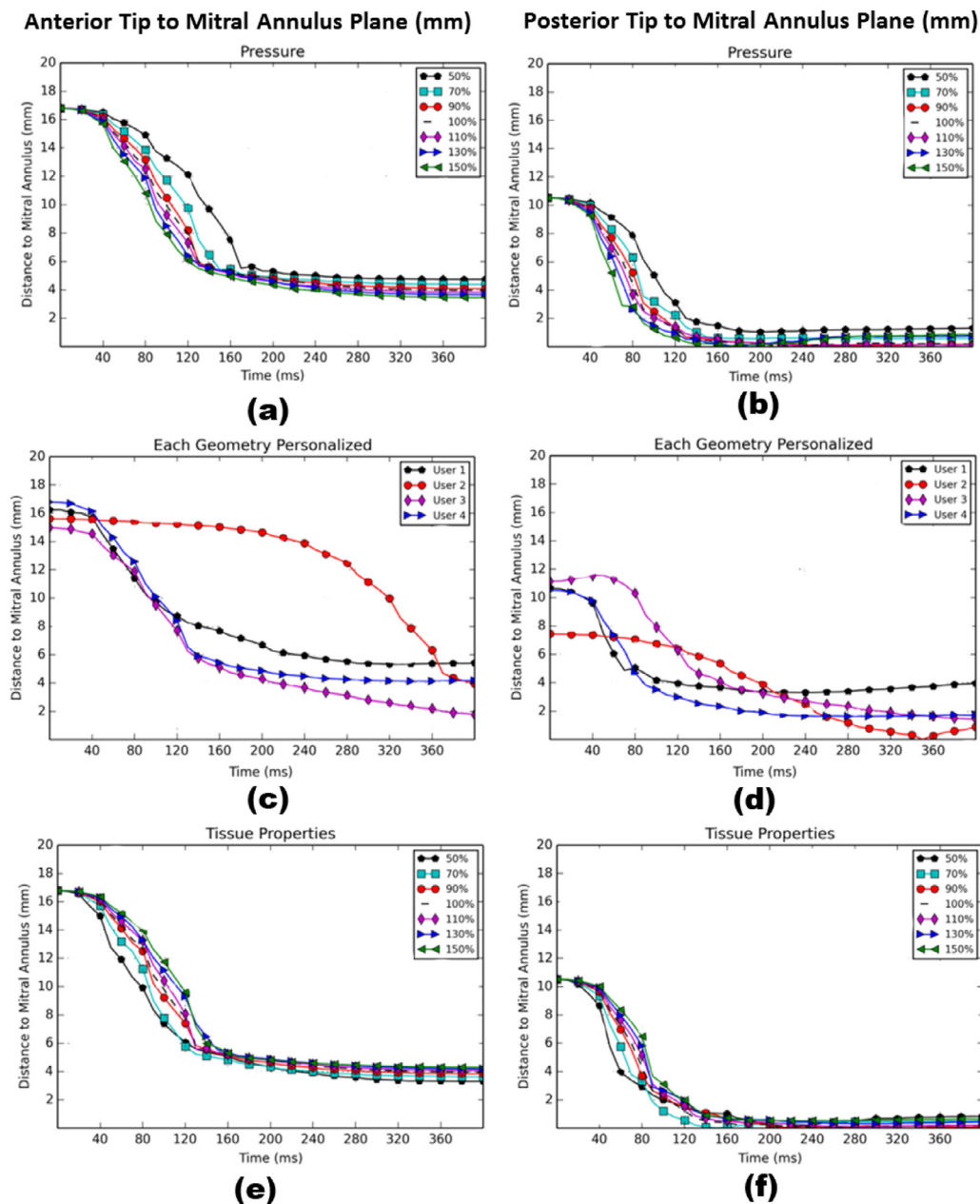


**Fig. 11.** Effect of parameters on the MV closure computation. The input MV geometry had a significant influence on the closure geometry while the impact of pressure and tissue properties (Young's Moduli) was minor.

improved chordae structures (see Fig. 5). Quantitative results on 10 cases show a significantly reduced point-to-mesh error of the computed MV closure geometry when compared to the ground-truth MV model from  $\mu$ CT. Results suggest that the physiologically appropriate hybrid sparse chordae representation produces similar results as the dense pseudo-chordae model. Thus there is no benefit in employing an over-represented pseudo-chordae topology and moving forward the hybrid model should be favored.

The sensitivity analysis showed that geometric parameters have a significant effect on MV closure computation. Thus, in order to get reproducible results, it is crucial to have either an automated method to retrieve MV models from the images (Ionasec et al., 2010; Grbic et al., 2012; Voigt et al., 2011) or a manual system used by trained expert raters (echocardiographers).

The inter-rater variability study suggests that there is deviation of the manual MV annotation between different raters, espe-

cially in the annular and coaptation region. Automation in the form of automated segmentation algorithms (Ionasec et al., 2010; Grbic et al., 2012; Schneider et al., 2012; Pouch et al., 2014) could be used in order to reduce inter-rater variability. It should be noted that despite being based on ultrasound, obtained in vitro Echo images might be slightly different from clinically-obtained in vivo Echo images. Therefore, the results of the sensitivity analysis cannot be directly translated to the clinical setup; a dedicated in vivo study would be necessary.

The MV closure computation using the two novel biomechanical models showed significant improvement compared to the previous MV model (Mansi et al., 2012) ( $p < 0.005$  for both the dense and hybrid chordae model). In addition the error of the computed MV closure model (2.24 mm for dense chordae model and 2.21 mm point-to-mesh error for the hybrid chordae model) is within the 95% confidence interval (2.58 mm point-to-mesh error)

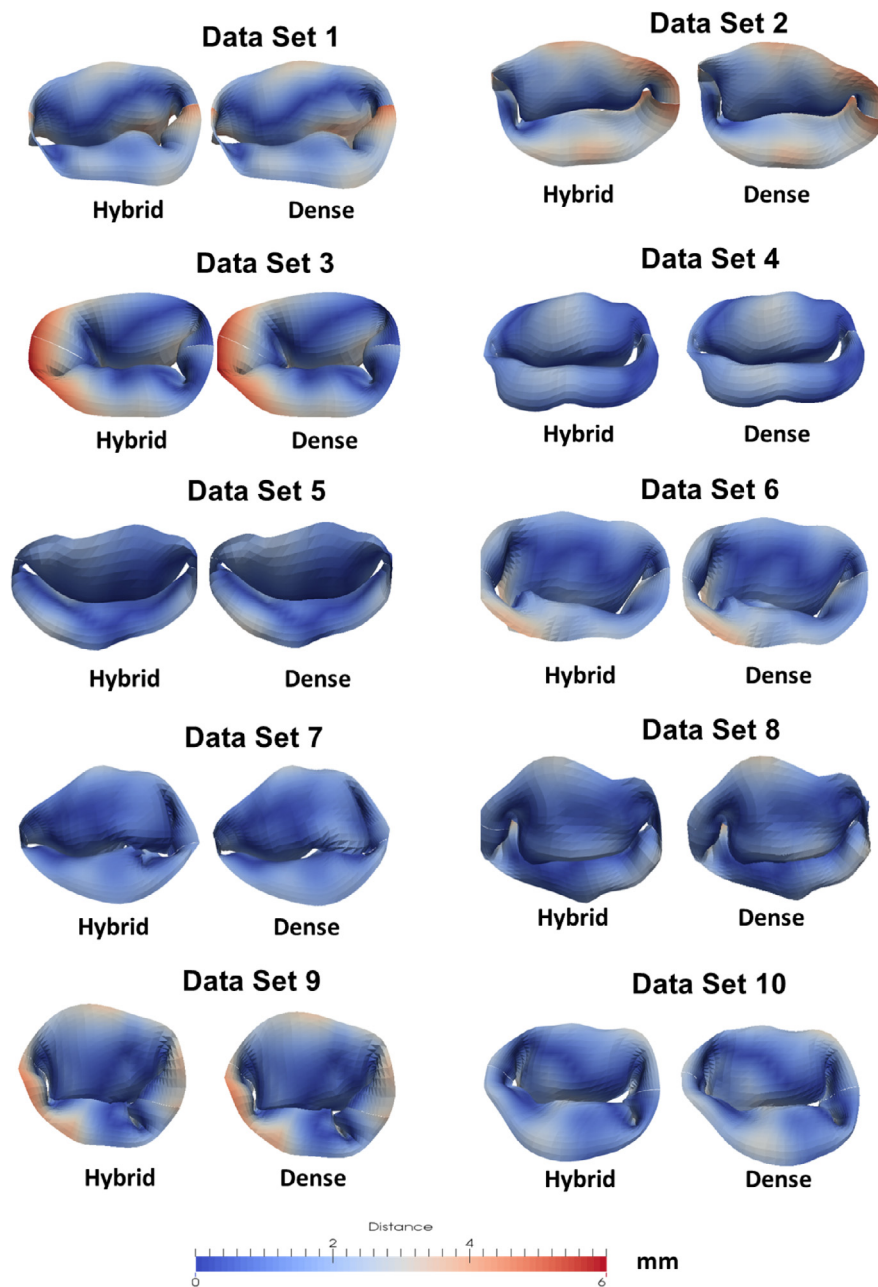


**Fig. 12.** Qualitative comparison of MV geometry from simulated Echo closure (Sim Echo) with dense (right) and hybrid sparse-dense pseudo-chordae representation (left) and the ground-truth  $\mu$ CT model. Point-to-mesh distance is color coded on the Sim Echo model.

of the inter-rater variability while the previous model was above (2.71 mm point-to-mesh error).

Personalization of important biomechanical parameters, such as chordae rest length, is essential to achieve acceptable MV closure results. Trust region optimization methods can be effectively used to remove the need for tedious and time-consuming manual personalization. Future directions will involve optimization of an extended parameter set including leaflet stiffness, chordae spring stiffness and chordae topology.

As the geometric configuration of the MV in the unpressurized  $\mu$ CT does not correspond with the geometry in Echo during diastole, only the closed  $\mu$ CT image data was used in the comparisons. Without a pressure gradient, a suspension in liquid, and flow, the MV leaflets scrunch and become thicker. In addition, the chordae tendineae bunch and it was not possible to delineate the full MV chordae tendineae topology. However, with applied air pressure

the leaflet fibers expand to the same geometric configuration as seen in Echo. Experimental innovations to reduce these adverse open/air scan phenomena were under active investigation. In this study a linear elastic material was used to simulate the passive properties of MV leaflets. While co-rotational FEM helped to cope with large deformations, the non-linear response of the tissue was neglected. Several other studies made the same modeling assumptions (Schievano et al., 2009; Krishnamurthy et al., 2009; Hammer et al., 2011), yielding convincing simulations. In parallel, more precise non-linear tissue models have been derived from ex-vivo stress-strain experiments (May-Newman and Yin, 1998; Prot et al., 2009; Lee et al., 2015; Stevanella et al., 2011).

In this work, the main focus was on the performance of different MV chordae models. It had been shown that these boundary conditions drive most of the MV motion (Mansi et al., 2012; Prot et al., 2009). In a future study, an impact analysis of tissue

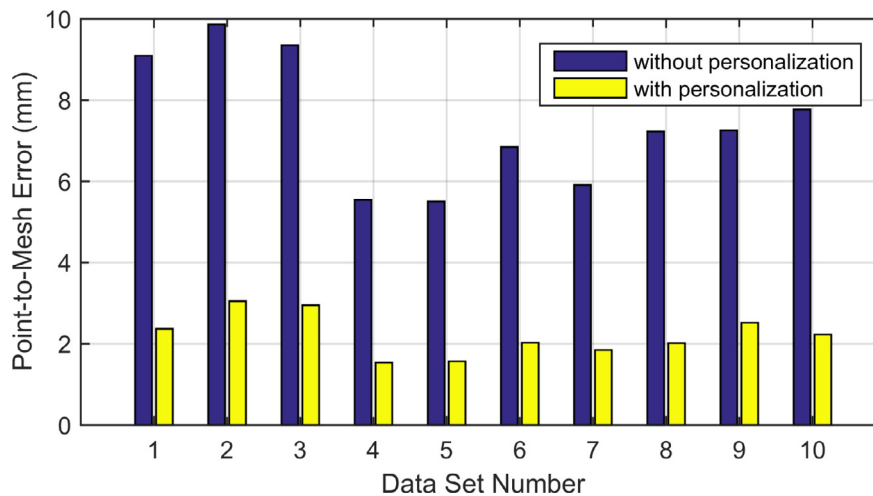


**Fig. 13.** Mean point-to-mesh distance between the simulated closure model computed using the MV biomechanical model with hybrid sparse-dense pseudo-chordae representation and the ground truth  $\mu$ CT model. The result was compared using generic values of 11.06 mm (mean chordae rest length of all personalized models) for all the chordae rest length parameters ( $B_{Ant}$ ,  $M_{Ant}$ ,  $B_{Post}$ ,  $M_{Post}$ ) - blue - and after personalization - yellow. (For interpretation of the references to color in this figure legend, the reader is referred to the web version of this article).

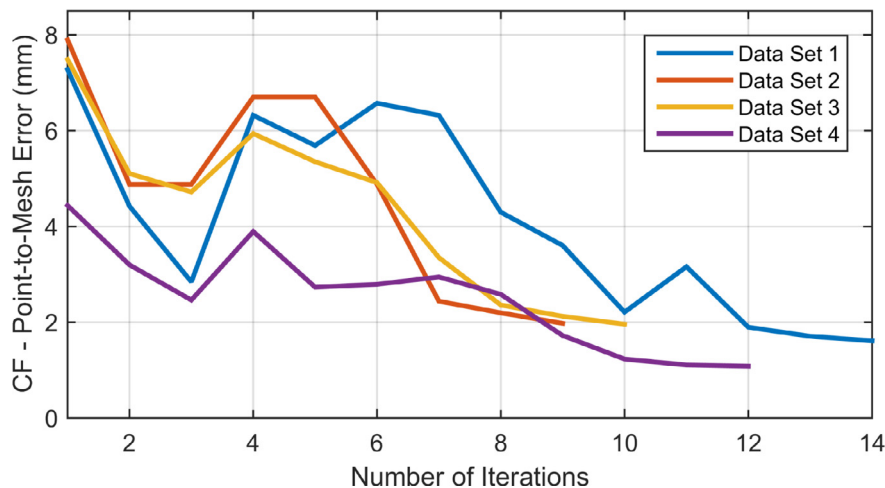


**Fig. 14.** Cost function (CF) progression during the trust region optimization with BOBYQA for four data sets.

non-linearity using novel FEM solvers will be conducted, allowing for fast computation; this was a necessary requirement for inverse modeling (Zettinig et al., 2013).

Currently the computational model was evaluated only on healthy ovine valves with no prolapse or incomplete closure. In future studies, the focus will be on validating the models with incomplete closure and using simple MVR techniques, such as the edge-to-edge repair and annuloplasty. The proposed computational model should predict the acute post-repair MV geometry and function.

## 5. Conclusion

In this study a novel MV model was introduced that utilizes two novel chordae representations capable of approximating regional connectivity between MV leaflets and chordae tendinae, showing a significant improvement in accuracy in closure computation when compared to the simplified parachute model (Mansi et al., 2012). The hierarchical personalization framework of the rest length parameters removes the need for tedious manual parameter selection. A controlled in vitro setup was utilized with 10 ovine data sets to quantify the performance of the computational model in predicting MV closure based on a biomechanical models de-

rived from Echo images. Initial results were promising, suggesting that the biomechanical model derived from Echo could be accurate enough to model basic geometric characteristics of MV function. The next step is to extend the study for predictive modeling where diseased MV function can be simulated and validated.

## Acknowledgments

This study was supported by grants from the Food and Drug Administration (FDA-SOL-1119843 and FDA-SOL-1119844).

## References

- Allard, J., Cotin, S., Faure, F., Bensoussan, P.-J., Poyer, F., Duriez, C., Delingette, H., Grisoni, L., 2007. Sofa-an open source framework for medical simulation. In: MMVR 15-Medicine Meets Virtual Reality, 125. IOP Press, pp. 13–18.
- Aspert, N., Santa Cruz, D., Ebrahimi, T., 2002. Mesh: measuring errors between surfaces using the hausdorff distance. In: ICME, 1, pp. 705–708.
- Bolling, S.F., Li, S., O'Brien, S.M., Brennan, J.M., Prager, R.L., Gammie, J.S., 2010. Predictors of mitral valve repair: clinical and surgeon factors. *Ann. Thorac. Surg.* 90 (6), 1904–1912.
- Borger, M.A., Alam, A., Murphy, P.M., Doenst, T., David, T.E., 2006. Chronic ischemic mitral regurgitation: repair, replace or rethink? *Ann. Thorac. Surg.* 81 (3), 1153–1161.

- Braunberger, E., Deloche, A., Berrebi, A., Abdallah, F., Celestin, J., Meimoun, P., Chatellier, G., Chauvaud, S., Fabiani, J., Carpentier, A., 2001. Very long-term results (more than 20 years) of valve repair with carpentier's techniques in non-rheumatic mitral valve insufficiency. *Circulation* 104 (suppl 1), 1–8.
- Comas, O., Taylor, Z.A., Allard, J., Ourselin, S., Cotin, S., Passenger, J., 2008. Efficient nonlinear fem for soft tissue modelling and its gpu implementation within the open source framework sofa. In: *Biomedical Simulation*. Springer, pp. 28–39.
- Gammie, J.S., Sheng, S., Griffith, B.P., Peterson, E.D., Rankin, J.S., O'Brien, S.M., Brown, J.M., 2009. Trends in mitral valve surgery in the united states: results from the society of thoracic surgeons adult cardiac database. *Ann. Thorac. Surg.* 87 (5), 1431–1439.
- Grbic, S., Easley, T.F., Mansi, T., Bloodworth, C.H., Pierce, E.L., Voigt, I., Neumann, D., Krebs, J., Yuh, D.D., Jensen, M.O., et al., 2015. Multi-modal validation framework of mitral valve geometry and functional computational models. In: *Statistical Atlases and Computational Models of the Heart-Imaging and Modelling Challenges*. Springer International Publishing, pp. 239–248.
- Grbic, S., Ionasec, R., Vitanovski, D., Voigt, I., Wang, Y., Georgescu, B., Navab, N., Comaniciu, D., 2012. Complete valvular heart apparatus model from 4d cardiac ct. *Med. Image Anal.* 16 (5), 1003–1014.
- Grbic, S., Mansi, T., Ionasec, R., Voigt, I., Houle, H., John, M., Schoebinger, M., Navab, N., Comaniciu, D., 2013. Image-based computational models for tavi planning: From ct images to implant deployment. In: *Medical Image Computing and Computer-Assisted Intervention-MICCAI 2013*. Springer Berlin Heidelberg, pp. 395–402.
- Hammer, P.E., Pedro, J., Howe, R.D., 2011. Anisotropic mass-spring method accurately simulates mitral valve closure from image-based models. In: *Functional Imaging and Modeling of the Heart*. Springer, pp. 233–240.
- Ho, S., 2002. Anatomy of the mitral valve. *Heart* 88 (suppl 4), iv5–iv10.
- Ionasec, R.I., Voigt, I., Georgescu, B., Wang, Y., Houle, H., Vega-Higuera, F., Navab, N., Comaniciu, D., 2010. Patient-specific modeling and quantification of the aortic and mitral valves from 4-d cardiac ct and tee. *Med. Imaging IEEE Trans.* 29 (9), 1636–1651.
- Jimenez, J.H., Soerensen, D.D., He, Z., Ritchie, J., Yoganathan, A.P., 2005. Effects of papillary muscle position on chordal force distribution: an in-vitro study. *J. Heart Valve Dis.* 14 (3), 295–302.
- Jones, E.C., Devereux, R.B., Roman, M.J., Liu, J.E., Fishman, D., Lee, E.T., Welty, T.K., Fabsitz, R.R., Howard, B.V., 2001. Prevalence and correlates of mitral regurgitation in a population-based sample (the strong heart study). *Am. J. Cardiol.* 87 (3), 298–304.
- Kanik, J., Mansi, T., Voigt, I., Sharma, P., Ionasec, R.I., Comaniciu, D., Duncan, J., 2014. Automatic personalization of the mitral valve biomechanical model based on 4d transesophageal echocardiography. In: *Statistical Atlases and Computational Models of the Heart. Imaging and Modelling Challenges*. Springer, pp. 162–170.
- Kilic, A., Shah, A.S., Conte, J.V., Baumgartner, W.A., Yuh, D.D., 2013. Operative outcomes in mitral valve surgery: combined effect of surgeon and hospital volume in a population-based analysis. *J. Thorac. Cardiovasc. Surg.* 146 (3), 638–646.
- Krishnamurthy, G., Itoh, A., Bothe, W., Swanson, J., Kuhl, E., Karlsson, M., Craig Miller, D., Ingels, N., 2009. Stress-strain behavior of mitral valve leaflets in the beating ovine heart. *J. Biomech.* 42 (12), 1909–1916.
- Kunzelman, K., Cochran, R., Chuong, C., Ring, W., Verrier, E., Eberhart, R., 1993. Finite element analysis of the mitral valve. *J. Heart Valve Dis.* 2 (3), 326–340.
- Lee, C.-H., Rabbah, J.-P., Yoganathan, A.P., Gorman, R.C., Gorman III, J.H., Sacks, M.S., 2015. On the effects of leaflet microstructure and constitutive model on the closing behavior of the mitral valve. *Biomech. Model. Mechanobiol.* 14 (6), 1281–1302.
- Mansi, T., Voigt, I., Georgescu, B., Zheng, X., Mengue, E.A., Hackl, M., Ionasec, R.I., Noack, T., Seeburger, J., Comaniciu, D., 2012. An integrated framework for finite-element modeling of mitral valve biomechanics from medical images: application to mitralclip intervention planning. *Med. Image Anal.* 16 (7), 1330–1346. Special Issue on the 2011 Conference on Medical Image Computing and Computer Assisted Intervention. <http://dx.doi.org/10.1016/j.media.2012.05.009>.
- May-Newman, K., Yin, F., 1998. A constitutive law for mitral valve tissue. *J. Biomech. Eng.* 120 (1), 38–47.
- Nkomo, V.T., Gardin, J.M., Skelton, T.N., Gottdiener, J.S., Scott, C.G., Enriquez-Sarano, M., 2006. Burden of valvular heart diseases: a population-based study. *Lancet* 368 (9540), 1005–1011.
- Pouch, A.M., Wang, H., Takabe, M., Jackson, B.M., Gorman, J., Gorman, R.C., Yushkevich, P.A., Sehgal, C.M., 2014. Fully automatic segmentation of the mitral leaflets in 3d transesophageal echocardiographic images using multi-atlas joint label fusion and deformable medial modeling. *Med. Image Anal.* 18 (1), 118–129.
- Pouch, A.M., Yushkevich, P.A., Jackson, B.M., Jassar, A.S., Vergnat, M., Gorman, J.H., Gorman, R.C., Sehgal, C.M., 2012. Development of a semi-automated method for mitral valve modeling with medial axis representation using 3d ultrasound. *Med. Phys.* 39 (2), 933–950.
- Powell, M.J., 2009. The bobyqa algorithm for bound constrained optimization without derivatives. Cambridge NA Report NA2009/06. University of Cambridge, Cambridge.
- Prot, V., Haaverstad, R., Skallerud, B., 2009. Finite element analysis of the mitral apparatus: annulus shape effect and chordal force distribution. *Biomech. Model. Mechanobiol.* 8 (1), 43–55.
- Rabbah, J.-P., Saikrishnan, N., Yoganathan, A.P., 2013. A novel left heart simulator for the multi-modality characterization of native mitral valve geometry and fluid mechanics. *Ann. Biomed. Eng.* 41 (2), 305–315.
- Roger, V.L., Go, A.S., Lloyd-Jones, D.M., Adams, R.J., Berry, J.D., Brown, T.M., Carnethon, M.R., Dai, S., de Simone, G., Ford, E.S., et al., 2011. Heart disease and stroke statistics?2011 update a report from the american heart association. *Circulation* 123 (4), e18–e209.
- Schievano, S., Kunzelman, K., Nicosia, M., Cochran, R., Einstein, D., Khambadkone, S., Bonhoeffer, P., 2009. Percutaneous mitral valve dilatation: single balloon versus double balloon. A finite element study. *J. Heart Valve Dis.* 18 (1), 28–34.
- Schneider, R.J., Perrin, D.P., Vasilyev, N.V., Marx, G.R., Pedro, J., Howe, R.D., 2012. Mitral annulus segmentation from four-dimensional ultrasound using a valve state predictor and constrained optical flow. *Med. Image Anal.* 16 (2), 497–504.
- Siefert, A.W., Rabbah, J.P.M., Koomalsingh, K.J., Touchton, S.A., Saikrishnan, N., McGarvey, J.R., Gorman, R.C., Gorman, J.H., Yoganathan, A.P., 2013. In vitro mitral valve simulator mimics systolic valvular function of chronic ischemic mitral regurgitation ovine model. *Ann. Thorac. Surg.* 95 (3), 825–830.
- Stevanella, M., Maffessanti, F., Conti, C.A., Votta, E., Arnoldi, A., Lombardi, M., Parodi, O., Caiani, E.G., Redaelli, A., 2011. Mitral valve patient-specific finite element modeling from cardiac MRI: application to an annuloplasty procedure. *Cardiovasc. Eng. Technol.* 2 (2), 66–76.
- Stewart, S., MacIntyre, K., Capewell, S., McMurray, J., 2003. Heart failure and the aging population: an increasing burden in the 21st century? *Heart* 89 (1), 49–53.
- Vassileva, C.M., McNeely, C., Spertus, J., Markwell, S., Hazelrigg, S., 2015. Hospital volume, mitral repair rates, and mortality in mitral valve surgery in the elderly: an analysis of us hospitals treating medicare fee-for-service patients. *J. Thorac. Cardiovasc. Surg.* 149 (3), 762–768.
- Vassileva, C.M., Mishkel, G., McNeely, C., Boley, T., Markwell, S., Scaife, S., Hazelrigg, S., 2013. Long-term survival of patients undergoing mitral valve repair and replacement a longitudinal analysis of medicare fee-for-service beneficiaries. *Circulation* 127 (18), 1870–1876.
- Voigt, I., Mansi, T., Ionasec, R.I., Mengue, E.A., Houle, H., Georgescu, B., Hornegger, J., Comaniciu, D., 2011. Robust physically-constrained modeling of the mitral valve and subvalvular apparatus. In: *Medical Image Computing and Computer-Assisted Intervention-MICCAI 2011*. Springer, pp. 504–511.
- Votta, E., Le, T.B., Stevanella, M., Fusini, L., Caiani, E.G., Redaelli, A., Sotiropoulos, F., 2013. Toward patient-specific simulations of cardiac valves: state-of-the-art and future directions. *J. Biomech.* 46 (2), 217–228.
- Wang, Q., Sun, W., 2013. Finite element modeling of mitral valve dynamic deformation using patient-specific multislices computed tomography scans. *Ann. Biomed. Eng.* 41 (1), 142–153.
- Zettinig, O., Mansi, T., Georgescu, B., Rapaka, S., Kamen, A., Haas, J., Frese, K.S., Sedaghat-Hamedani, F., Kayvanpour, E., Amr, A., et al., 2013. From medical images to fast computational models of heart electromechanics: an integrated framework towards clinical use. In: *Functional Imaging and Modeling of the Heart*. Springer, pp. 249–258.